ADVANCED FUNCTIONAL MATERIALS

DOI: 10.1002/adfm.200600349

Gold-Nanoparticle-Doped TiO_2 Semiconductor Thin Films: Optical Characterization**

By *Dario Buso*, *Jessica Pacifico*, *Alessandro Martucci*, and *Paul Mulvaney**

A simple procedure for creating titania sol–gel-based semiconductor thin films is described. Gold nanoparticles are doped homogeneously into the precursor mixture and the particles are homogeneously distributed in the resultant films when prepared using spin-coating. The effects of particle loading and annealing temperature on the optical properties of the resultant films are characterized. Ellipsometry, X-ray diffraction, atomic force microscopy, and surface plasmon spectroscopy are used to monitor the crystallization and porosity changes during film synthesis.

1. Introduction

There has been a recent resurgence of interest in metal-nanoparticle-doped dielectric matrices, spurred on by new applications in diverse fields ranging from nonlinear optics[1,2] and photocatalytic pollutant degradation[3,4] through to gas sensing.[5–7] The original work in this field was motivated by the unusual optical properties of small metal particles and led to the development of powerful, effective medium models to handle the complex material properties of nanocomposites. However, current applications involve tuning not only the optical and electronic properties of the composite material, but also the matrix architecture. For example, in photocatalysis and gas sensing, the matrix must be porous enough for gases to diffuse through the matrix to active sites, undergo chemical reaction, and exit the film. Thus, it is no longer sufficient to measure the average dielectric properties of the nanoparticle-doped films; it is also necessary to characterize the particle distribution within the film and the role of the pore volume. A further important shift has been the emergence of sol–gel methods that are more flexible than conventional glass technologies and enable much lower processing temperatures to be utilized.

In the majority of sol–gel syntheses, the metal is introduced in the form of a soluble salt, then reduced to form small metal particles in situ through annealing, gaseous reduction, or through photochemical reactions,[3,8–10] although there are some alternative strategies for particle doping such as ion implantation[11,12] and sputtering.[1] However, all these physical and chemical methods suffer the same inherent limitations: there is very limited control of the nucleation process, the final particle size, the particle polydispersity, and the particle shape. An alternative approach that offers more flexibility in the design and fabrication of nanoparticle-doped dielectrics is to synthesize the nanoparticles using optimized routes in conventional chemical batch reactors and then to introduce them into the sol–gel precursor. Some of the advantages of ex situ nanoparticle synthesis are: 1) The ability to dope the matrix with core/shell particles. 2) The ability to incorporate particles of different shape, for example nanorods. 3) The opportunity to tailor the surface chemistry, e.g., passivation of defect or recombination sites. 4) The chance to carry out size-selection and purification of the particles. 5) The potential to derivatize the nanoparticles, for example by functionalization with redox acceptors, donors, dyes, or even with other metal-semiconductor composite nanoparticles (NPs).

In this study, we report on the fabrication of gold-nanoparticle-doped titania dielectric matrices using monodisperse gold nanoparticles. We discuss pathways for homogeneous integration of the particles into the film and discuss how the optical properties change during annealing. It is further shown that ex situ synthesis and doping can lead to homogeneous distributions of nanoparticles, and the method can be readily extended to other nanoparticles. There is a complex interplay between matrix crystallization, porosity, and composite refractive index that can be monitored using surface plasmon shifts or spectroscopic ellipsometry. In subsequent papers, we will correlate the optical properties with the electronic properties and gas diffusion behavior of the nanoparticle-doped films.

2. Results

Figure 1 summarizes the overall synthetic procedure adopted to obtain homogeneously Au-NP-doped TiO_2 films

[*] Prof. P. Mulvaney, D. Buso, Dr. J. Pacifico, Prof. A. Martucci
School of Chemistry
University of Melbourne
Parkville, VIC 3010 (Australia)
E-mail: mulvaney@unimelb.edu.au
D. Buso, Prof. A. Martucci
Dipartimento di Ingegneria Meccanica S. Materiali
Università di Padova
Via Marzolo, 9, 35131 Padova (Italy)

[**] Alessandro Martucci thanks the Universities of Melbourne and Padova for their support through the University academic exchange program, and MIUR through PRIN 2004 project. Jessica Pacifico is supported through ARC Grant DP 0558608. Paul Mulvaney thanks the University of Melbourne and the ARC for support through the Federation Fellowship program. This paper is the first in a series discussing gold-nanoparticle-doped TiO_2 semiconductor thin films.

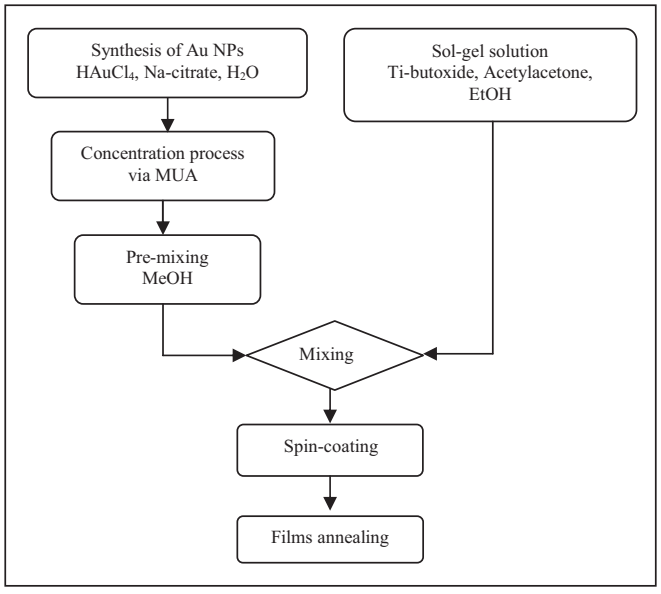

Figure 1. Scheme of the overall synthetic process developed to dope TiO_2 sol–gel thin films with morphologically controlled Au NPs. Control of the Au nanoparticle morphology is obtained by separating the particle synthesis from the TiO_2 sol–gel process.

(see Experimental section for details). Gold NPs (500 mL, 0.50 mM) in water were synthesized using the Turkevich method.[13] In order to phase transfer the particles into ethanol, they were first functionalized by addition of mercaptoundecanoic acid (1 mM in ethanol) at pH 7. The mercaptan was allowed to adsorb over half an hour, then the pH was lowered to pH 3 using 1 M HCl. The particles were allowed to sediment overnight, then centrifuged and washed to remove all unreacted salts and spectator ions. Finally, the black precipitate was repeptized into a minimum volume of water (ca. 5 mL) with 20 μL of NH_3 (28 vol %). Separately, a sol–gel solution containing the TiO_2 precursor was prepared by mixing titanium butoxide, 2,4-pentanedione (acetylacetone, AcAcH), and EtOH (ethanol). To facilitate the dispersion of the Au NPs into the sol–gel solution, the concentrated Au suspension in water was premixed with MeOH (methanol; $MeOH/H_2O = 3:1$) and then added to the sol–gel Ti butoxide solution. The pH of the Au NP suspension in water after the concentration procedure was around 8, decreasing to 7 after addition of MeOH. The starting sol–gel solution had a pH in the range of 6–7, while the final solution (Au NPs in water/MeOH/sol–gel solution) was pH 5.

In Figure 2, an electron microscopy image of the Au nanoparticles is shown. The size distribution was determined using ImageJ 1.34s picture analyzer software[14] to analyze 600 particles. The particles had a mean diameter of 9.7 nm with standard deviation of 0.9 nm as depicted in the upper inset of Figure 2. Optical absorption spectra of the same suspension diluted 1:600 are visible in the lower inset of Figure 2. The narrow absorption peak centered at 520 nm is the typical band associated with the surface plasmon resonance (SPR) of conduction electrons in gold small spherical clusters. The extinction coefficient ε ($M^{-1}\,cm^{-1}$) was found[15] to be 3995 $M^{-1}\,cm^{-1}$ at $\lambda = 522$ nm, leading to a gold-particle concentration of 61.4×10^{-3} M after concentration and surface functionalization.

Absorption spectra of TiO_2 and TiO_2–Au films over the 200–800 nm range for samples heated from 100 °C up to 500 °C are reported in Figure 3. Each panel reports absorption spectra of both Au-doped (solid line) and undoped films (dashed line) at each annealing temperature. The SPR band resulting from the gold nanoparticles in TiO_2–Au films is clearly visible in each film. The dotted vertical line marks the SPR peak of the Au clusters in the initial aqueous solution (522 nm); as expected, there is a clear red-shift when the gold particles are embedded in the TiO_2 matrix because of the higher refractive index of the sol–gel matrix.[16] Optical absorbance spectra of undoped TiO_2 films are also presented in each panel as dashed lines and show no evidence for the surface plasmon band associated with gold particles. There is however a broad absorption band centered at 800 nm in the 100 °C annealed sample that steadily blue-shifts to 375 nm after annealing at 500 °C, which results from optical interference.

The effect of particle concentration on the surface plasmon resonance is shown in Figure 4. The peak absorption is directly proportional to gold content for films annealed at all tempera-

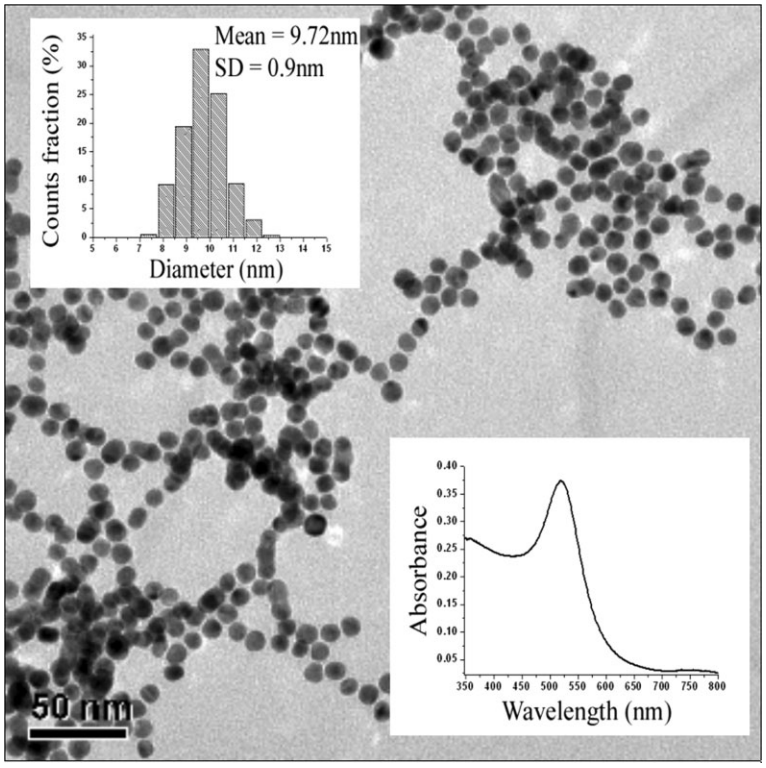

Figure 2. Bright-field transmission electron microscopy (TEM) image showing Au nanocrystals as synthesized in water. Upper inset reports the particle size distribution evaluated using ImageJ software. The mean particle size is 9.72 nm (0.9 nm standard deviation (SD)). Lower inset shows optical absorption spectra of the same NP suspension with a surface plasmon resonance (SPR) band at 522 nm.

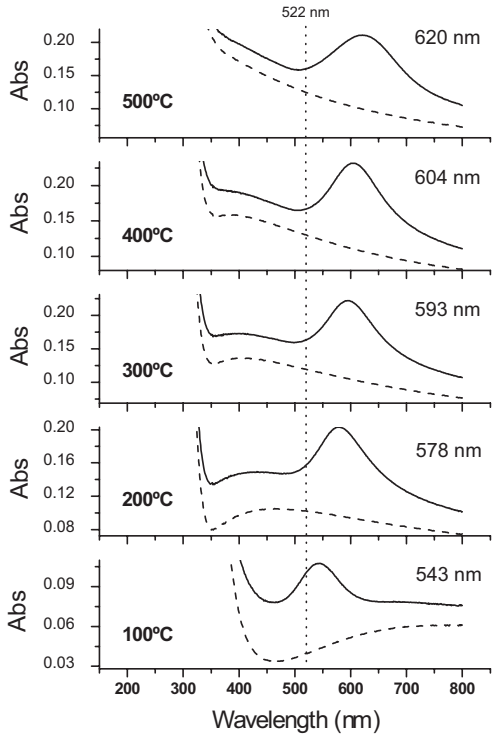

Figure 3. Optical absorption spectra (solid lines) of Au doped TiO_2 films annealed at temperatures in the 100–500 °C range (reported on the left side of the panels). For comparison, the dotted vertical line marks the position of the SPR band at 522 nm obtained for Au NPs in water. The position of the maximum of the SPR band of Au NPs in TiO_2 red-shifts with increasing annealing temperatures to wavelengths reported on the right side of each panel. Absorption spectra reported with dashed lines are for blank TiO_2 films.

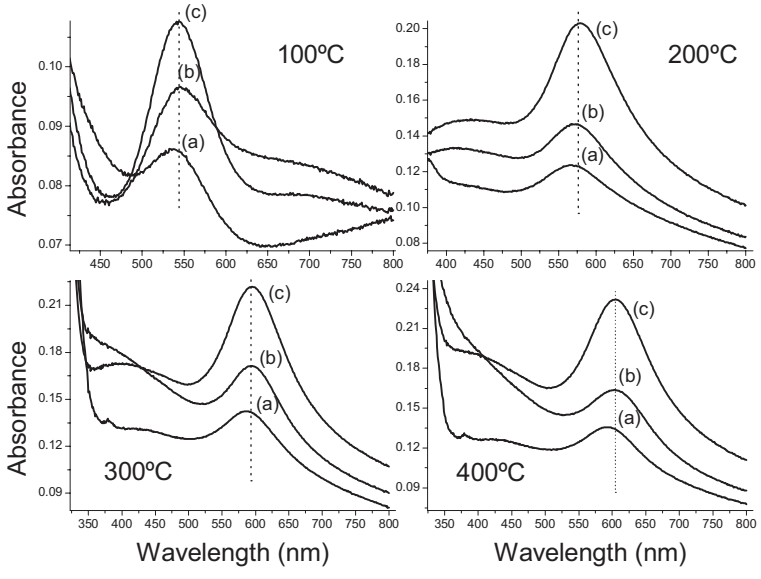

Figure 4. Absorption spectra of TiO_2–Au films heated in the 100–400 °C range (temperatures reported in panels). Each panel reports optical absorption spectra of TiO_2 films doped with three different Au NP weight fractions: a) 4 wt %, b) 5.5 wt %, c) 8 wt %.

tures except 100 °C. Because the gold volume fraction is low, the SPR peak position does not change with doping concentration. The primary parameter that affects the peak position is the annealing temperature.

In Figure 5, the peak position of the SPR band is plotted as a function of the annealing temperature of the samples for films with different Au particle concentrations. The progressive red-shift of the maximum wavelength is proportional to the increase in the annealing temperature of the sample and follows

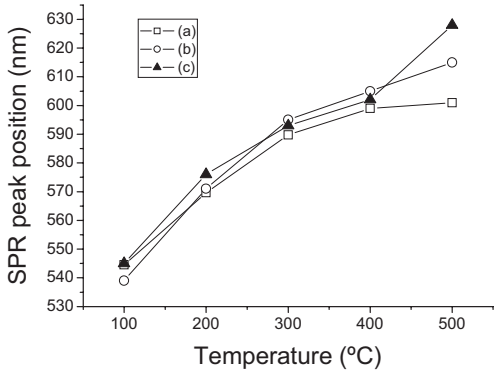

Figure 5. Evolution of the observed red-shift position of the SPR band maximum for TiO_2–Au films versus annealing temperature in the 100–500 °C range. The lines reported refer to three different Au NP concentrations: a) 4 wt %, b) 5.5 wt %, c) 8 wt %. PL: photoluminescence.

a similar trend for films with different gold content up to 400 °C, whereas for films annealed at 500 °C the data points are spread over a wider range of wavelengths. The position predicted by Mie theory for 10 nm particles in crystalline anatase is 648 nm. Hence, the average matrix refractive index approaches the values of the crystalline bulk semiconductor only after extensive high-temperature annealing.

An important question is whether there is significant particle migration during spin-coating or during annealing of the semiconductor films. To investigate this, the sol–gel precursor was spin-coated onto the reverse side of a carbon-coated copper transmission electron microscopy (TEM) grid and subsequently annealed at 200 °C. The 50 nm thick film was then imaged directly in the electron microscope. The image in Figure 6 shows a homogeneous dispersion of Au nanoparticles over micrometer-length scales. In a few isolated cases, some small aggregates can be discerned, as shown in the inset. However the overwhelming majority of particles remain well-separated and statistically dispersed. Size distribution analysis performed with ImageJ 1.34s yielded a mean particle size value of 9.51 nm with a standard deviation of 0.89 nm, in close agreement with the results obtained from the TEM image of particles in the initial water solution.

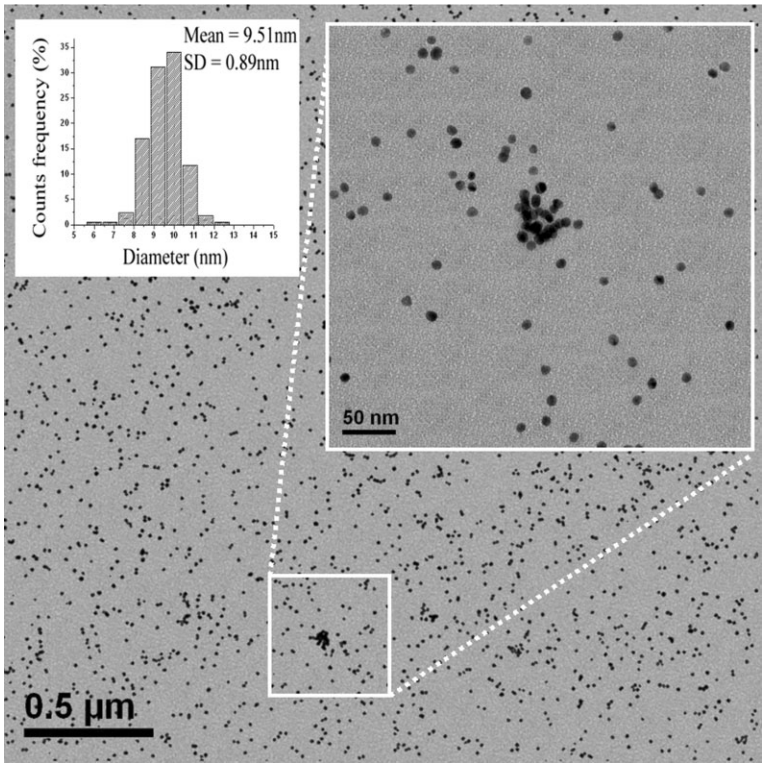

Figure 6. Large-scale bright-field TEM image of a TiO_2–Au (8 wt%) film deposited on the back side of a carbon-coated copper grid and annealed at 200 °C. A histogram of the size distribution of the particles is reported in the upper left inset. Calculated mean particle diameter is 9.51 nm (0.89 nm SD). The inset on the right reports a close-up view of an Au NP aggregate.

The images in Figure 8 show four samples of TiO_2 and TiO_2–Au films deposited on silica substrates and annealed at the reported temperatures. The sample dimensions can be deduced from the scale at the bottom. Undoped films (upper samples) are colorless across the whole annealing temperature range (only the samples annealed at 100 °C and 400 °C are shown in the picture) while the TiO_2 Au films evince pink to violet colors depending on the firing temperature.

The X-ray diffraction (XRD) spectra reported in Figure 9 show the microstructural composition of TiO_2–Au films annealed at 200, 400, and 500 °C together with the diffraction signal from a monolayer of Au particles deposited on an aminopropylsilane-functionalized glass slide. The peaks detectable in all the patterns arise from (111) and (200) planes of the cubic lattice of crystalline metal gold (powder diffraction file no. 04-0784, International Centre for Diffraction Data (ICDD), Newton Square, PA). The crystal size evaluated from the Scherrer equation using the full width at half maximum (FWHM) values of the diffraction peaks are spread around a mean value of 5 nm with a maximum deviation of 8 %. However the titania film exhibits no discernible diffraction peaks at temperatures up to 400 °C. Only when annealed at 500 °C does crystallization into the anatase phase occur, leading to peaks from (101) and (200) lattice planes (powder diffraction file no. 86-1157, ICCD), with calculated mean crystal dimensions of 11 nm.

The film topography was analyzed by atomic force microscopy (AFM) to determine if the annealing and crystallization affect the overall film smoothness, which is critical for optical applications. In Figures 10a,b and 11a–c, typical tapping mode images are shown, and Figures 10c and 11d report topographic profiles obtained from the images. Figure 10d

In Figure 7 the refractive indices of the films that underwent annealing at increasing temperatures are plotted together with the calculated refractive index using the peak position of the SPR band. The *y*-axis on the right side reports the film porosity calculated using the refractive indices of the film.

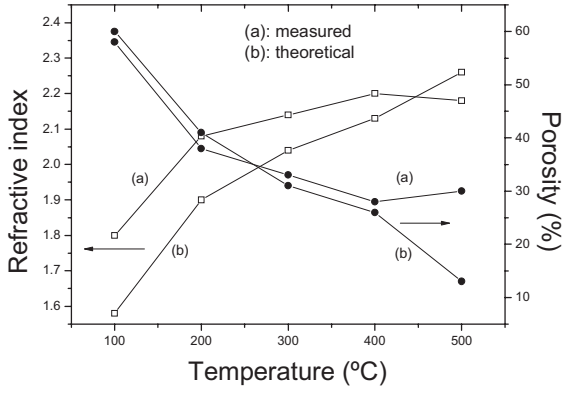

Figure 7. Thermal evolution of TiO_2–Au (8 wt%) film refractive indices (left *y*-axis) and porosity (right *y*-axis) a) measured by ellipsometry and b) calculated with the Mie theory using the SPR band maximum of Au NPs.

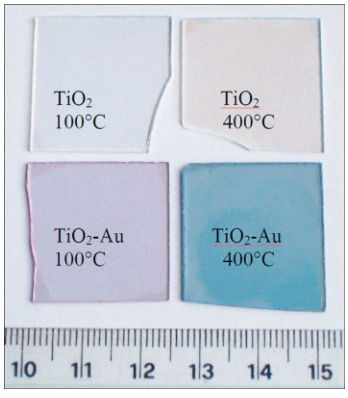

Figure 8. Picture of TiO_2 films (upper) and TiO_2–Au (8 wt%) films (lower) deposited on SiO_2 glass substrates annealed at 100 °C (left side) and 400 °C (right side). The scale bar is in centimeters. Au NPs confer the films with a pinkish color after low-temperature annealing that turns to violet after treatment at higher temperatures.

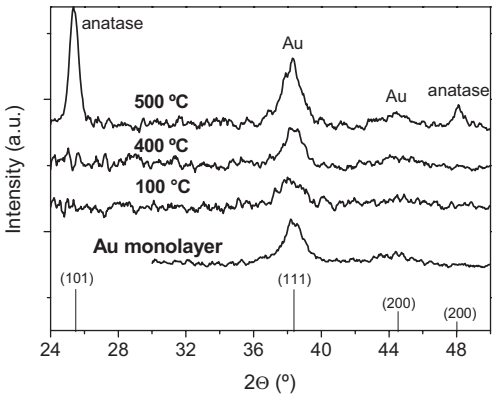

Figure 9. XRD pattern of films annealed from 100 to 400 °C and at 500 °C. Au(111) and (200) diffraction planes are recognizable in all the patterns, while anatase (101) and (200) lattice planes are detectable in films heated up to 500 °C. Crystalline grain dimensions evaluated with the Scherrer correlation yield a crystallite diameter of 5 nm for Au NPs and 11 nm for anatase. The lower plot is the diffraction pattern obtained from a pure Au NP monolayer deposited on (3-aminopropyl)triethoxysilane (APES) functionalised SiO_2 glass substrate. Peaks associated with the (111) and (200) lattice planes of metallic Au are visible. The grain size was estimated to be 5 nm.

shows the evolution of average peak-to-trough height of the surface features as a function of the annealing temperature of the sample, and Figure 11c shows the image obtained after a scan performed on an Au NP monolayer which was synthesized by adsorption of NPs onto (3-aminopropyl)triethoxysilane (APES)-functionalised glass surface.

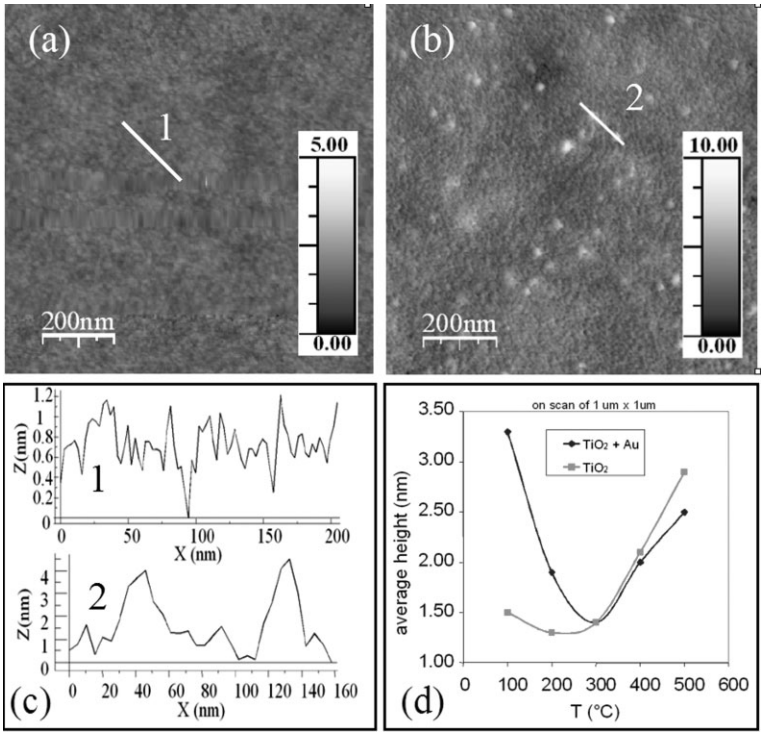

Figure 10. 1 μm × 1 μm AFM images of a) TiO_2 film and b) TiO_2–Au (8 wt%) film heated at 100 °C. Linear scans 1 and 2 are plotted in (c). d) Evolution of the average height versus temperature (100–500 °C range) for TiO_2 and TiO_2–Au films. White spots in (b) are Au NPs partially emerging from film surface. The mean *z*-direction surface roughness values evaluated from (a) and (b) are 0.3 and 0.8 nm, respectively.

3. Discussion

The key synthetic goal of this work was the design of a generic process for dispersing monodisperse metal nanoparticles into titania films over a wide range of particle concentrations with minimal aggregation or phase separation. A key step is the surface functionalization of the nanoparticles so that they can be highly concentrated and dispersed into ethanol-based solutions, which have a substantially lower dielectric constant than water. MUA-capped Au nanoparticles are highly soluble in basic aqueous environments and aggregate in acidic media because of protonation of the carboxyl groups of MUA.[15] Addition of 1 M HCl solution to the MUA/Au particles suspension in water causes the particles to flocculate and gently precipitate at the bottom of the flask allowing almost complete solvent removal. The consequent addition of 20 μL of concentrated NH_3 solution (28 vol%) causes fast ionization of the carboxylic groups and leads to complete repeptization without strongly increasing the ionic strength.[17]

Direct mixing of the citrate-stabilized aqueous Au suspension with the sol–gel solution is not possible because of rapid hydrolysis/condensation reactions of the Ti butoxide promoted by the water in the gold sol and because of rapid aggregation of the gold sol. It has been previously demonstrated that the carboxyl groups of MUA do not ionize in ethanol,[17] but only ethanol-based sol–gel solutions allow deposition of TiO_2 films of good optical quality. These issues can be obviated by addition of acetylacetone to the sol–gel solution, which retards the hydrolysis rate of Ti butoxide.[18] Furthermore in order to securely transfer the Au particles into the sol–gel mixture, methanol has been found to be a suitable carrier. Premixing the aqueous MUA-capped Au nanoparticle suspension with methanol prevents particle aggregation when the Au in the water/methanol mixture is added to the titanium butoxide solution in ethanol. This may be related to the difference in polarity of methanol (32.6 at 25 °C[19]) and ethanol (24.3 at 25 °C[19]). However, ethanol is the preferred solvent since rapid evaporation of methanol induces undesired Au-particle aggregation and even expulsion of particles from the matrix.[8]

More difficult to identify is the optimal pH of the precursor solution. Titania has a point of zero charge (PZC) in aqueous media of pH 5.5–6.8, depending on the particle crystallinity and the anions present,[14,20,21] because of protonation and deprotonation of surface hydroxyl groups to form $Ti–OH_2^+$ species at pH < PZC or $Ti–O^-$ groups at pH > PZC.

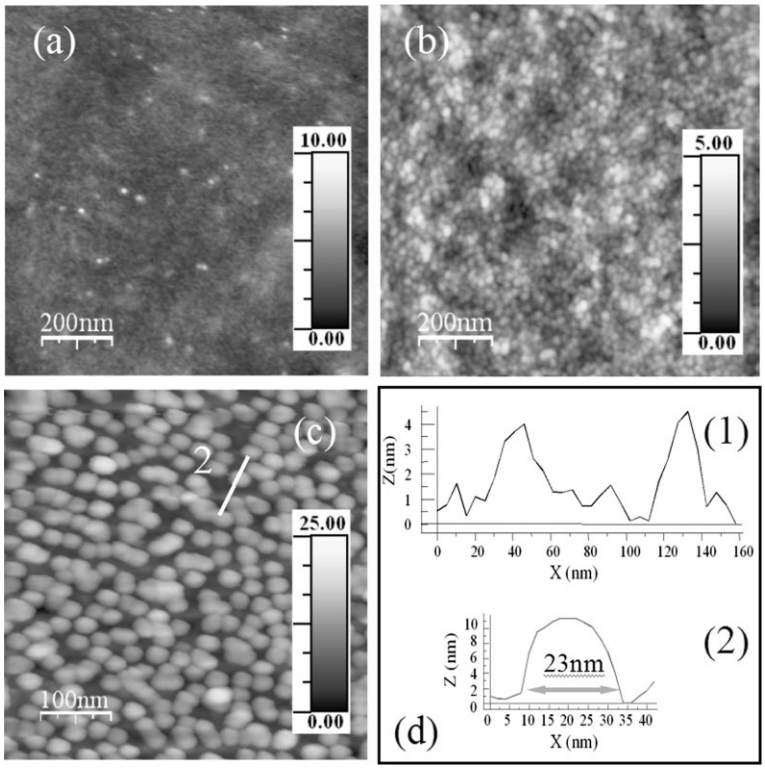

Figure 11. a) 1 μm × 1 μm AFM image of a TiO_2–Au film annealed at up to 300 °C. b) 1 μm × 1 μm AFM image of a TiO_2–Au film surface heated to 500 °C. The grainy structure of anatase crystals is discernible over the whole region. c) 0.5 μm × 0.5 μm image of a Au NP monolayer deposited on the surface of a SiO_2 substrate: Well-separated, "naked", single particles are recognizable. d) Topographical traces of gold particles 1) on top of a gold doped titania film and 2) on top of a silica substrate. The maximum vertical excursion in (1) is 4 nm, while in (2) it is 11 nm.

The decreasing pH of the solutions used in the synthesis scheme (Fig. 1) from 8 to 5 can be ascribed to the chemistry of the overall process. The basic character of the concentrated Au/MUA suspension in water results from the dissociation of NH_3 to form NH_4^+ and OH^-. Approximately 6 % of the total amount of NH_3 molecules ionize the carboxylic terminal groups of MUA, stabilizing Au NPs in the aqueous environment. The pH is reduced to about 7 when an excess of methanol is added, probably because the lower dielectric constant reduces the degree of ionization of the ammonia. Nevertheless, MUA-stabilized Au NPs do not aggregate when methanol is added (whereas they do aggregate if ethanol or longer carbon chain alcohols are added), indicating that the carboxyl groups of the MUA are still partially ionized in methanol. When the sol–gel solution is added, the pH of the mixture further decreases because of deprotonation of acetylacetone by ammonia in the aqueous solution; a known reaction that is adopted as an effective method for the chemical synthesis of β-amino ketones.[22,23] The pH value (around 5) of the final sol–gel solution is lower than the PZC for TiO_2, thus conferring a weak but significant positive charge density on the TiO_2 surface that can effectively anchor the negatively charged Au nanoparticles. Consequently, the pH values that allow controlled, homogeneous nanoparticle loading are confined to a small pH range (between 5 and 6.8). The higher limit is imposed by the necessity of ensuring the final sol–gel solution has a pH lower than the PZC of TiO_2, while the lower one is necessary to avoid aggregation of Au NPs.[15]

The optical absorbance spectra of Figure 3 clearly show a red-shift of the absorption plasmon band of Au NPs inside the TiO_2 films depending on the annealing temperature. It must be mentioned that all the TiO_2–Au films were synthesized from the same batch of Au clusters; moreover, the TEM images in Figure 6 demonstrate that the Au particles are not affected by the annealing process and do not aggregate inside the matrix. Consequently, any observed change in the optical absorption spectra can be attributed to differences in the TiO_2 refractive index. The optical absorption spectra in Figure 4 further corroborate the assertion that the red-shift of the SPR band is associated with a modification of the optical properties of the matrix and not to changes in the particle morphology, because the wavelength of the SPR band maximum remains unvaried if films with different gold contents are annealed at the same temperature.

Spectroscopic ellipsometry has been used to measure the optical constants and film thickness of all the samples (see Table 1). The refractive index can also be determined independently from the position of the SP band using Equation 1

$$\lambda_{max}^2 = \lambda_p^2(\varepsilon_\infty + 2\varepsilon_m) \quad (1)$$

Here, λ_p is the bulk plasma wavelength of gold (131 nm) and ε_∞ is the high frequency value of the dielectric function (12.2 for gold). For a nonabsorbing matrix, the refractive index is $n_{med} = \sqrt{\varepsilon v}$. Measured values of the refractive index of the TiO_2–Au films are plotted in Figure 7 (left *y*-axis) together with the values calculated using Equation 1.[24] The maximum difference between the calculated values and the measured ones is about 10 % for the samples annealed at 100 °C. The right side of the graph in Figure 10 reports the film porosity estimated using the refractive indices of the films (both measured

Table 1. Film thicknesses and refractive indices (*n*) measured using ellipsometry at 589 nm for TiO_2 and TiO_2–Au (8 wt %) films at different annealing temperatures measured using ellipsometry.

Annealing Temperature [°C]	Film thickness [nm]		Refractive index, *n*	
	TiO_2	TiO_2–Au	TiO_2	TiO_2–Au
100	82	99	1.75	1.80
200	48	58	2.06	2.08
300	48	48	2.09	2.14
400	42	42	2.19	2.20
500	41	42	2.17	2.18

ADVANCED FUNCTIONAL MATERIALS

and calculated) using the equation proposed by Zhao et al.[25] and Ahn et al.[26] and assuming a value of $n = 2.52$ for the refractive index of dense TiO_2. The measured thicknesses and refractive indices of both TiO_2 and TiO_2–Au films are summarized in Table 1. While the refractive indices calculated from the SP-band position are consistently lower than the values from ellipsometry, the difference is not large. The simplest explanation for the difference is that ellipsometry measures the volume-average refractive index, including the void space and the sol–gel matrix, whereas the gold nanoparticles may interact locally with regions of slightly lower-than-average refractive index. We exclude changes to the gold particle optical properties since the dielectric data of Johnson and Christy have been found to be very accurate for the region $1.3 < n < 1.6$.[27] Furthermore, there is no evidence for thermally induced shape changes that would cause red-shifts,[15,28] nor is there evidence for polydispersity.[9,15] The porosity values of the titania films calculated both from measured and estimated n_{med} values are in close agreement except for samples heated at 500 °C.

XRD analysis performed on TiO_2–Au films allows the microstructural evolution of the films during the annealing process to be monitored. Figure 9 reports diffraction peaks registered for TiO_2–Au films annealed at 100, 400, and 500 °C as well as measurements of a gold NP monolayer deposited on a silica glass substrate by means of APES. The XRD signal arising from Au NPs embedded in TiO_2 matrices is identical to the one obtained from the naked Au NP monolayer on a glass surface, showing peaks from (111) and (200) planes of the Au lattice and the same FWHM. The grain size calculated from the XRD spectrum was found to be 5–6 nm; as the mean particle diameter estimated using TEM is 9.51 nm we can conclude that the particles are nearly monocrystalline. Conversely, XRD spectra of films annealed at 500 °C show peaks belonging to crystalline anatase (101) and (200) lattice planes, indicating that the phase transition from amorphous titania to anatase occurs between 400 °C and 500 °C. At this annealing temperature, the size of the anatase grains estimated with the Scherrer equation is 11 nm.

AFM scans of the film surface were used to monitor the film structure and morphology. 1 μm × 1 μm scans revealed an extremely smooth surface topography, with values of the average surface roughness in the 0.3–0.6 nm and 0.3–0.8 nm ranges for TiO_2 and TiO_2–Au films, respectively. The trend of these values with annealing temperatures was different for Au-doped and undoped films. The roughness of pure TiO_2 films increased with increasing heating temperature of films, while for TiO_2–Au films the roughness was at a minimum for samples annealed at temperatures up to 300 °C. These trends are more evident in the line scans shown in Figure 10c. In Figure 10d, the average peak-to-trough height is plotted for films annealed at different temperatures. A comparison of the images in Figure 10a and b reveals that some gold nanoparticles are discernible as white spots on the sample surface in TiO_2–Au films. This causes the differences in the line scans, with the presence of 15 nm gold particles on the film surface causing larger surface roughness. However, above 300 °C, both Au-doped and undoped films exhibited increasing roughness, which must result from changes in the titania matrix. Studies conducted on TiO_2 surfaces[29,30] have revealed that for $T > 300$ °C an increase in surface roughness corresponds with the transformation of amorphous TiO_2 to the rougher polycrystalline phase of anatase. From these AFM measurements it can be deduced that the initial anatase grains forming at temperatures up to about 400 °C are probably too small to be effectively detected by XRD but are big enough to affect the surface topography of both TiO_2 and TiO_2–Au films.

A question that arises from these AFM scans is whether the emerging Au NPs visible on TiO_2–Au films are phase separating out of the TiO_2 network or are covered by a thin layer of TiO_2, and consequently totally embedded inside the matrix. To clarify this point a monolayer of Au NPs was deposited on a glass substrate by means of APES and then characterized by AFM. Figure 11a (amorphous TiO_2–Au film) and b (crystalline TiO_2–Au film) clearly reveal the differences in surface morphology induced by TiO_2 crystallization. After annealing at 500 °C, anatase grains are clearly recognizable with AFM, and Au NPs are no longer easily resolved because the grain size of the anatase and gold are very much alike. These images of anatase with grain size of 10–12 nm are consistent with the mean grain size of 11 nm calculated from the Scherrer equation.

In Figure 11c, an AFM image of a dense gold nanoparticle monolayer is shown. The particles can be readily identified despite close packing. A cross section through a single particle is shown in Figure 11d. The gold particle is readily identified by its almost spherical profile. Despite the close packing of the particles, the target nanoparticle sits about 10–12 nm above the surrounding matrix. The apparent width of 23 nm is an aberration caused by the finite tip angle.[31] We conclude that if the particles were phase separated from the titania during crystallization, they would present much higher profiles on the film surface. The much lower, rougher profiles are more consistent with the particles remaining coated by titania, even if they migrate towards the surface.

Finally, we note that the broadening of the SPR in the films annealed at 500 °C may result from electronic interactions that occur between anatase and the metal clusters.[32] The interactions can induce spatial spreading and scattering of conduction electrons across the particle/matrix interface, modifying the electron density at the interfacial region,[10] thus resulting in broadening of the SPR band. The FWHM of the XRD peaks belonging to the Au lattice planes in the films annealed at 300–500 °C is constant, and this implies that there is no modification in grain features of Au NPs in TiO_2–Au films annealed at 500 °C.

4. Conclusions

We have demonstrated that small metal nanoparticles can be homogeneously dispersed into titania thin films using sol–gel processing. The optical properties of the resultant films depend on the annealing regimen, which determines the condensation and crystallization kinetics of the composite. The absorption scales linearly with particle loading, i.e., there is no surface

plasmon coupling in the films because of the low volume fraction of nanoparticles. Spin-coating directly onto TEM grids enables us to demonstrate that nanoparticle migration is minimal in films annealed at up to 300 °C. AFM reveals that the gold nanoparticles are exuded from the film during annealing. A similar process has been observed for gold–silica composites. Finally for photocatalysis and gas-sensing applications, it has been found that the surface plasmon resonance gives an accurate measure of the film porosity, which must be optimized for mass-transfer processes within the films.

5. Experimental

For the preparation of the colloidal gold dopant solution, $HAuCl_4$, trisodium citrate, analytical grade NH_3 (28 % aqueous solution), HCl (36 % aqueous solution), and mercaptoundecanoic acid (MUA, 95 %) were used as received. The water used was Milli-Q water at 18 MΩ. Titanium(IV) butoxide and 2,4-pentanedione (acetylacetone, AcAcH) were used as sol–gel. The overall synthetic route is summarized in the scheme of Figure 1. Colloidal gold was synthesized by reducing $HAuCl_4$ with trisodium citrate in water [13]. 40 mL of 1 % trisodium citrate solution was added to a 1 L boiling solution of 4.5×10^{-4} M $HAuCl_4$. The reaction was maintained at boiling point until a red-wine color of solution was observed. Separately, MUA was dissolved in a 2.5 vol % aqueous NH_3 solution to yield a 1×10^{-3} M concentration. The MUA solution was then added to the colloidal gold (25 μM) and incubated for 2 h under constant stirring at room temperature. 1 M HCl solution was then added dropwise to reduce the pH ~ 3, at which point the gold particles flocculated and started to precipitate to the bottom of the flask. There was a sudden change in color of the solution from wine-red to dark-violet. The suspension was sedimented overnight, then the supernatant was removed and the dense sediment (ca. 5 mL) was redispersed by simply adding a single drop (ca. 20 μL) of 28 vol % aqueous ammonia solution. The sol was then diluted to a final stock concentration of 60 mM.

Separately, titanium(IV) butoxide, 2,4-pentanedione, and EtOH were mixed at 1:1.6:1.2 mol ratios and allowed to react under stirring for 25 min in a closed vial. 2,4-Pentanedione complexes to the titanium(IV) butoxide molecules through a slight exothermic reaction, whereas EtOH decreases the overall viscosity of the solution. The concentrated gold suspension was diluted with MeOH and then mixed with the sol–gel solution in a volume ratio of gold colloid:MeOH:sol gel = 1:3:1. This was the solution used for film deposition.

Spin-coating was utilized for film deposition, and samples were obtained using both silica glass and silicon as substrates. Films were deposited at 3500 rpm for 25 s, at room temperature, and under a constant helium flux. Samples underwent thermal annealing in a tube furnace at temperatures progressively increasing from 100 to 500 °C, with a temperature gradient of 200 °C h^{-1}. Extinction spectra of nanoparticle solutions and films were collected using a Cary 5 UV-vis-NIR spectrometer in the 200–800 nm wavelength range. TEM images were taken using a Philips CM10 transmission electron microscope. The collection of an image of the gold-doped film was made possible by spin-coating a carbon-coated copper grid with the sol–gel solution. Ellipsometry was carried out using a Jobin-Yvon UVISEL spectroscopic ellipsometer and fitted to standard dispersion formulae. AFM imaging was carried out in tapping mode on a Digital Instruments Dimension 3100 instrument. All the films were characterized by X-ray diffraction (XRD) by using a Philips diffractometer equipped with glancing-incidence X-Ray optics. The analysis was performed using Cu Kα Ni-filtered radiation at 40 kV and 40 mA.

Received: April 18, 2006
Revised: June 16, 2006
Published online: January 10, 2007

[1] S. Cho, S. Lee, Soo-Ghee Oh, S. J. Park, W. M. Kim, Byung-Ki Cheong, M. Chung, K. B. Song, T. S. Lee, S. G. Kim, *Thin Solid Films* **2000**, *97*, 377.
[2] F. Hache, D. Richard, C. Flytzanis, K. Kreibig, *Appl. Phys. A* **1988**, *47*, 347.
[3] R. S. Sonawane, M. K. Donare, *J. Mol. Catal. A: Chem.* **2006**, *243*, 68.
[4] M. A. Aramendía, A. Marinas, J. M. Marinas, J. M. Moreno, F. J. Urbano, *Catal. Today* **2005**, *101*, 187.
[5] M. Z. Atashbar, H. T. Sun, B. Gong, W. Wlodarski, R. Lamb, *Thin Solid Films* **1998**, *326*, 238.
[6] R. M. Walton, D. J. Dwyer, J. W. Schwank, J. L. Gland, *Appl. Surf. Sci.* **1998**, *125*, 187.
[7] A. M. Ruiz, A. Cornet, K. Shimanoe, J. R. Morante, N. Yamazoe, *Sens. Actuators B* **2005**, *108*, 34.
[8] J. Matsuoka, H. Yoshida, H. Nasu, K. Kamiya, *J. Sol–Gel Sci. Technol.* **1997**, *9*, 145.
[9] S. K. Medda, S. De, G. De, *J. Mater. Chem.* **2005**, *15*, 3278.
[10] M. Lee, L. Chae, K. C. Lee, *Nanostruct. Mater.* **1999**, *11*, 195.
[11] G. W. Arnold, G. Battaglin, A. Boscolo-Boscoletto, P. Mazzoldi, C. Meneghini, *Mater. Res. Soc. Symp. Proc.* **1996**, *396*, 397.
[12] R. H. Magruder, III, L. Yang, R. F. Haglund, Jr., C. W. White, L. Yang, R. Dorsinville, R. R. Alfano, *Appl. Phys. Lett.* **1993**, *62*, 1730.
[13] B. V. Enüstün, J. Turkevich, *J. Am. Chem. Soc.* **1963**, *85*, 3317.
[14] ImageJ. http://rsb.info.nih.gov/ij (accessed September 2006).
[15] M. C. Daniel, D. Astruc, *Chem. Rev.* **2004**, *104*, 293.
[16] S. Underwood, P. Mulvaney, *Langmuir* **1994**, *10*, 3427.
[17] V. Kane, P. Mulvaney, *Langmuir* **1998**, *14*, 3303.
[18] D. Hoebbel, T. Reinert, H. Schmidt, *J. Sol–Gel Sci. Technol.* **1997**, *10*, 115.
[19] Dielectric Constants of Materials. http://www.clippercontrols.com/info/dielectric_constants.html (accessed September 2006).
[20] F. M. Vichi, M. I. Tejedor-Tejedor, M. A. Anderson, *Solid State Ionics* **2005**, *176*, 973.
[21] T. Oyama, A. Aoshima, S. Horikoshi, H. Hidaka, J. Zhao, N. Sermone, *Sol. Energy* **2004**, *77*, 525.
[22] M. J. Lacey, *Aust. J. Chem.* **1970**, *23*, 841.
[23] J. G. Stites, C. N. McCarthy, L. L. Quill, *J. Am. Chem. Soc.* **1948**, *70*, 3142.
[24] C. F. Bohren, D. F. Huffman, in *Absorption and Scattering of Light by Small Particles*, Wiley, New York **1983**.
[25] G. Zhao, S. Utsumi, H. Kozuka, T. Yoko, *J. Mater. Sci.* **1998**, *33*, 3655.
[26] Y. U. Ahn, E. J. Kim, H. T. Kim, S. H. Hahn, *Mater. Lett.* **2003**, *57*, 4660.
[27] J. Pérez-Juste, I. Pastoriza-Santos, L. M. Liz-Marzán, P. Mulvaney, *Coord. Chem. Rev.* **2005**, *249*, 1870.
[28] G. De, C. N. R. Rao, *J. Mater. Chem.* **2005**, *15*, 891.
[29] B. S. Richards, *Sol. Energy Mater. Sol. Cells* **2003**, *79*, 369.
[30] W. H. Wang, S. Chao, *Opt. Lett.* **1998**, *23*, 1417.
[31] M. Giersig, P. Mulvaney, *J. Chem. Soc., Faraday Trans.* **1996**, *32*, 3137.
[32] P. Alemany, R. S. Borse, J. M. Burlitch, R. Hoffmann, *J. Phys. Chem.* **1993**, *97*, 8464.